Electronic Supplementary Material (ESI) for Inorganic Chemistry Frontiers.

Supporting Information

Novel Ni–Ge–P anodes for lithium-ion batteries with enhanced reversibility and reduced redox potential

Guoping Liu,[a] Nan Wang,[b] Fangya Qi,[a] Xiaoyi Lu,[a] Yaohua Liang,[c] and Zhipeng Sun* [a]

[a] School of Materials and Energy, Guangdong University of Technology, Guangzhou 510006, China

[b] School of Materials & Energy, Lanzhou University, Gansu 730000, China

[c] Department of Agricultural and Biosystems Engineering, South Dakota State University, Brookings, South Dakota 57007, United States

* Corresponding author

Zhipeng Sun: zpsunxj@gdut.edu.cn

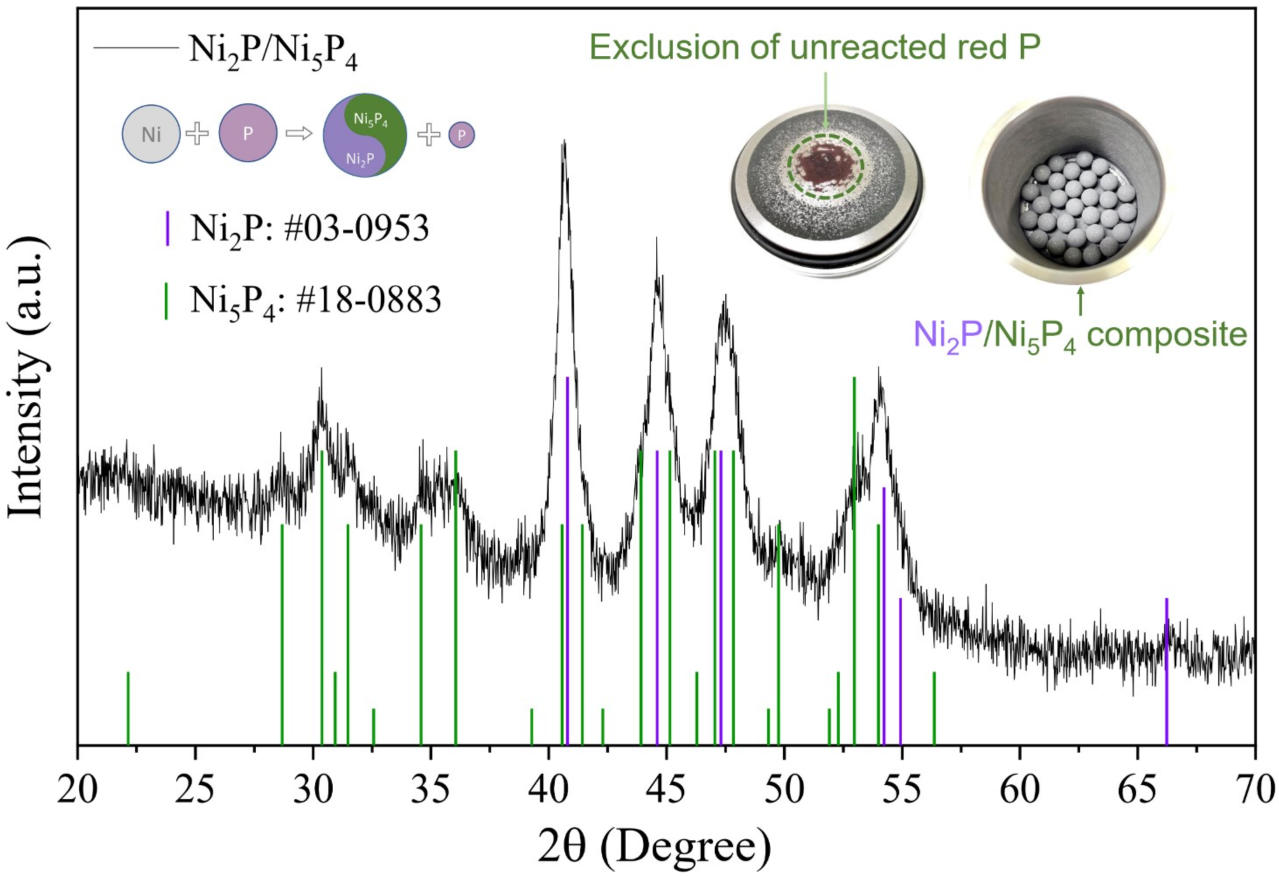

Fig. S1. The XRD result and the digital photo of the 14 h high-energy ball-milled Ni:P (1:1) mixed powder.

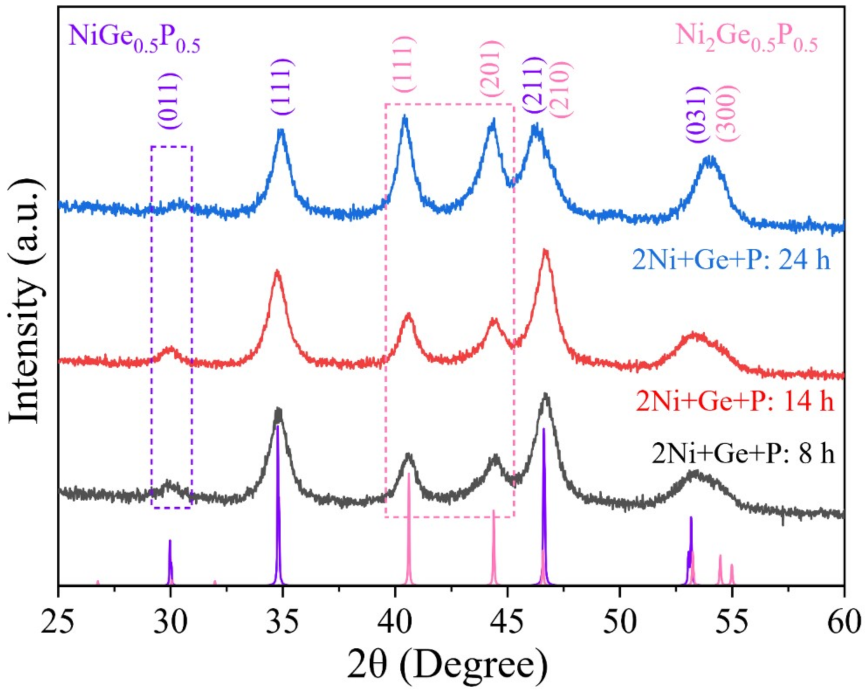

Fig. S2. The XRD pattern evolution of the ball-milled Ni: Ge: P (2: 1: 1) mixed powder after milling 8, 14, and 24 h.

Table S1. Structure parameters for Ni_2GeP/Ni_6Ge_2P as determined by Rietveld refinement of powder XRD data at room temperature.

$NiGe_{0.5}P_{0.5}$:

Atom	Wyckoff site	*x*/a	*y*/b	*z*/c	Occupancy
Ni	4a	0	0	0	1
Ge	4c	0.75	0.310	0	0.5
P	4c	0.75	0.310	0	0.5
Space group: Amam (63); *a* =5.1288 Å, *b* =5.9995 Å, *c* = 3.4286 Å, $\alpha = \beta = \gamma = 90°$, *wt.*% = 65.56%.					

$Ni_2Ge_{0.5}P_{0.5}$:

Atom	Wyckoff site	*x*/a	*y*/b	*z*/c	Occupancy
Ni1	3f	0.2580	0	0	1
Ni2	3g	0.5886	0	0.5	1
Ge1	1b	0	0	0.5	0.5
P1	1b	0	0	0.5	0.5
Ge2	2c	0.3333	0.6667	0	0.5
P2	2c	0.3333	0.6667	0	0.5
Space group: P-62m (189); *a* = *b* = 5.9077 Å, *c* = 3.3656 Å, $\alpha = \beta$ =90°, γ = 120°, *wt.*% = 34.44%.					

Table S2. Structure parameters for Ni_2P as determined by Rietveld refinement of powder XRD data at room temperature.

Atom	Wyckoff site	*x*/a	*y*/b	*z*/c	Occupancy
Ni1	3e	0.2575	0	0	1
Ni2	3f	0.5957	0	0.5	1
P1	1b	0	0	0.5	1
P2	2d	0.3333	0.6667	0	1
Space group: P321 (150); *a* = *b* = 5.8923 Å, *c* = 3.3478 Å, $\alpha = \beta$ =90°, γ = 120°.					

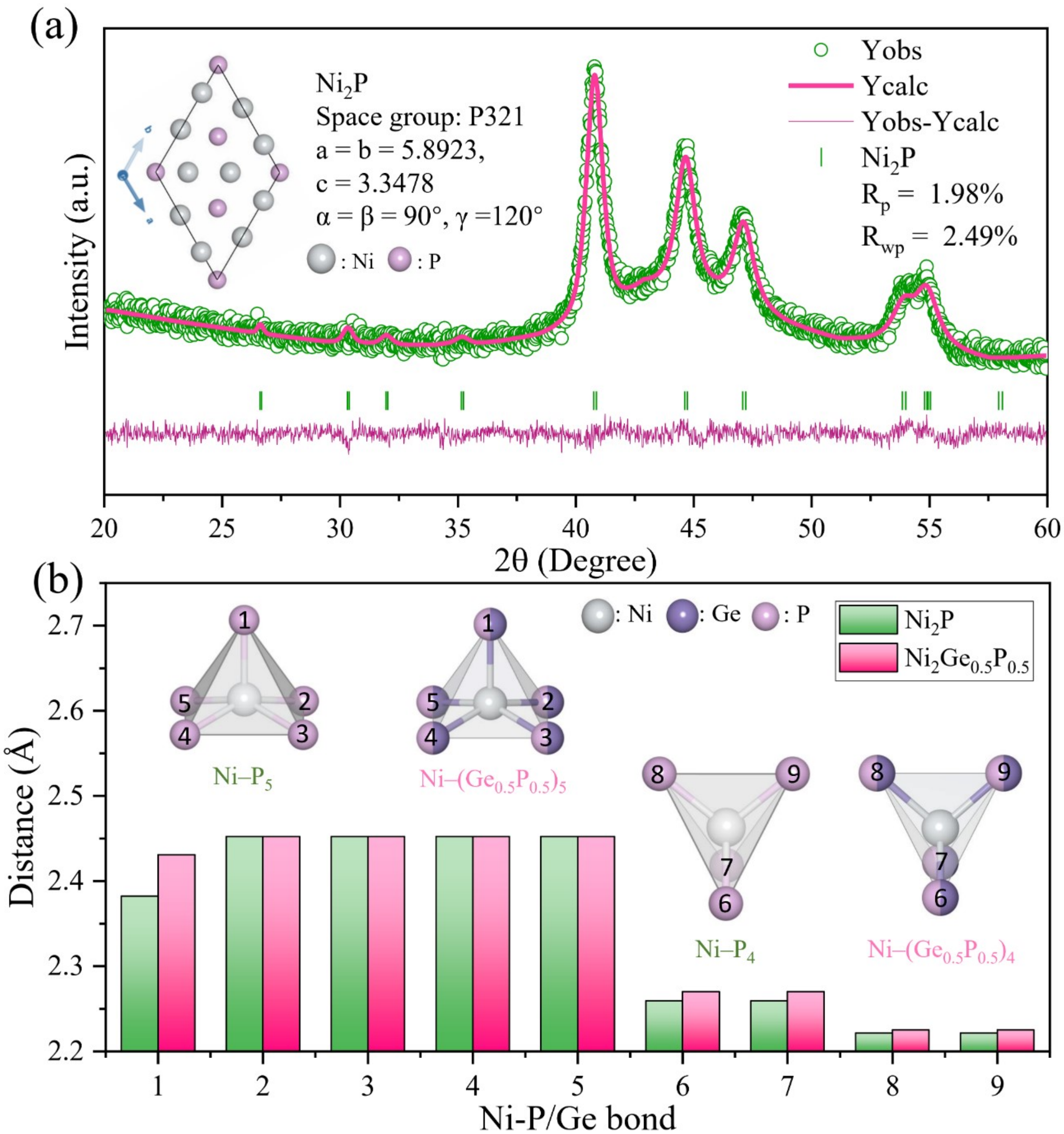

Fig. S3. (a) XRD refinement result of the Ni_2P. (b) The bond length of Ni–P/Ge in Ni–P_5, Ni–$(Ge_{0.5}P_{0.5})_5$, Ni–P_4, and Ni–$(Ge_{0.5}P_{0.5})_4$ polyhedron.

Table S3. Crystal structure parameters of NiP, $NiGe_{0.5}P_{0.5}$, Ni_2P, and $Ni_2Ge_{0.5}P_{0.5}$.

Phases	Space group	a (Å)	b (Å)	c (Å)	α	β	γ	Volume (Å^3)	Volume/Atom (Å^3)
NiP	Pbca	6.0500	4.8819	6.8900	90°	90°	90°	203.5	12.7
$NiGe_{0.5}P_{0.5}$	Amam	5.1288	5.9995	3.4286	90°	90°	90°	105.5	13.2
Ni_2P	P321	5.8923	5.8923	3.3478	90°	90°	120°	100.7	11.2
$Ni_2Ge_{0.5}P_{0.5}$	P-62m	5.9077	5.9077	3.3656	90°	90°	120°	101.7	11.3

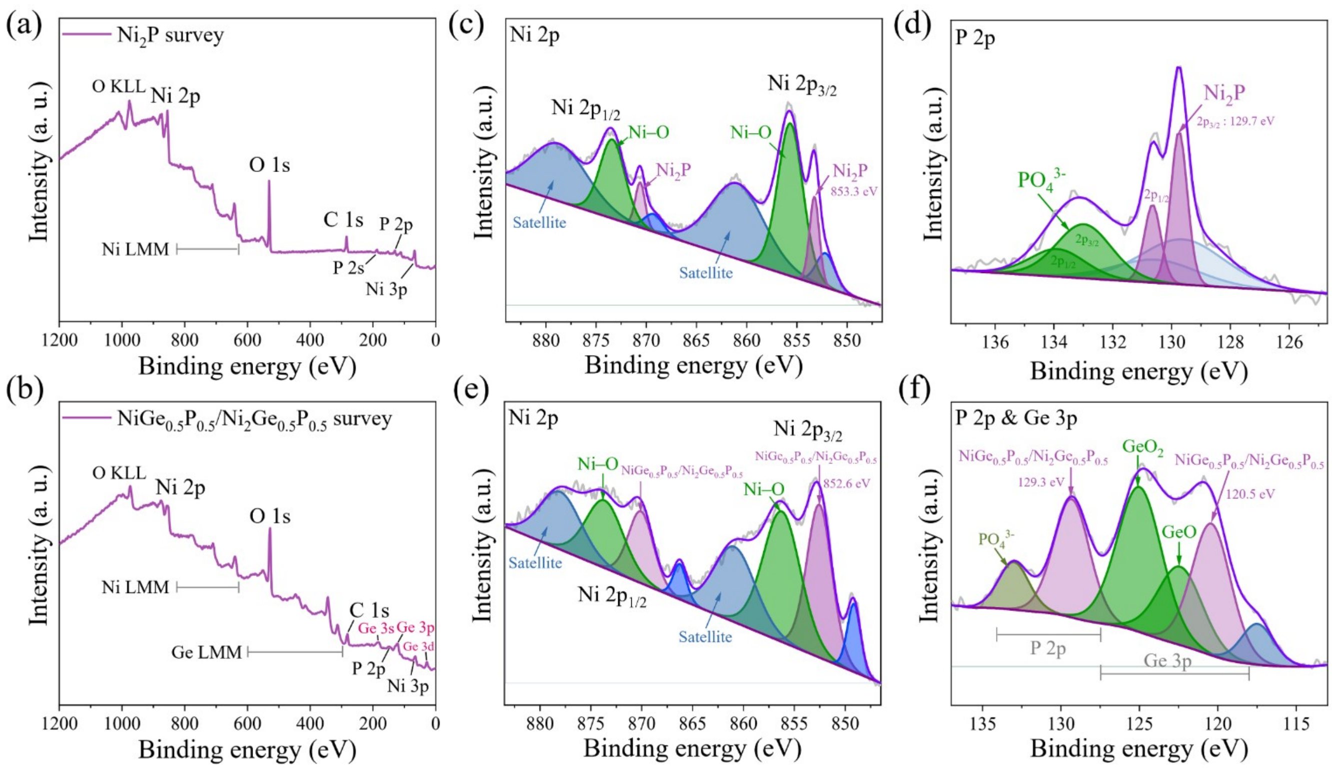

Fig. S4. Full XPS spectra of (a) Ni_2P and (b) $NiGe_{0.5}P_{0.5}/Ni_2Ge_{0.5}P_{0.5}$. (c) Ni 2p and (d) P 2p high-resolution XPS spectra of Ni_2P. (e) Ni 2p and (f) P 2p, Ge 3p high-resolution XPS spectra of $NiGe_{0.5}P_{0.5}/Ni_2Ge_{0.5}P_{0.5}$.

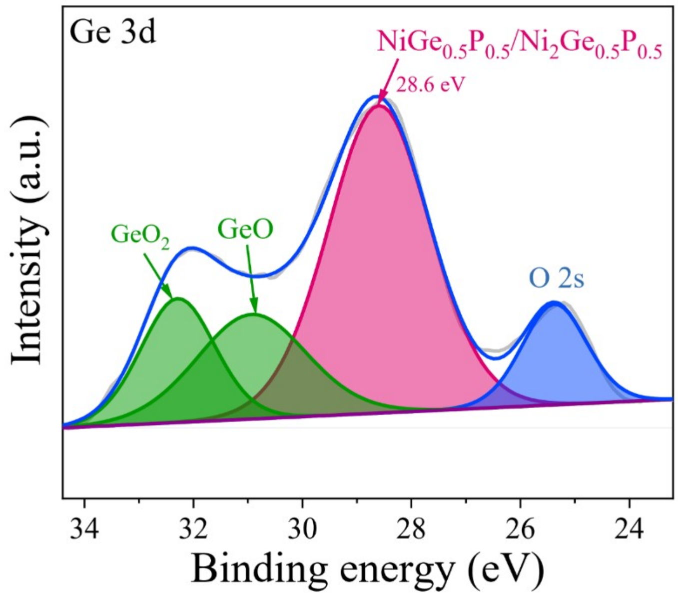

Fig. S5. The Ge 3d high-resolution XPS spectrum of Ni_2Gep/Ni_6Ge_2P.

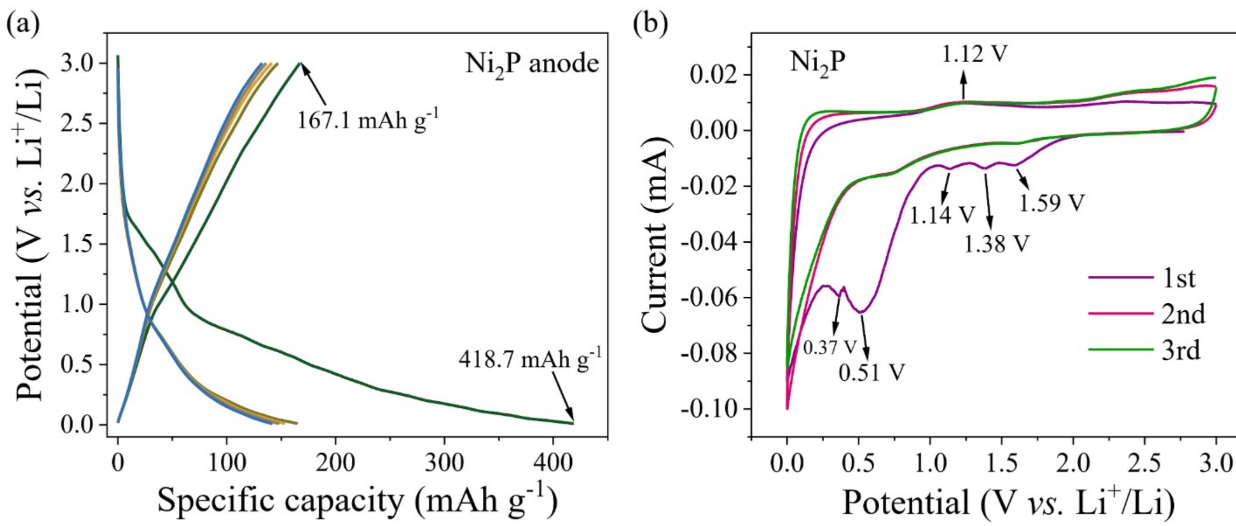

Fig. S6. Galvanostatic charge−discharge curves of Ni_2P composite at 50 mA g^{-1} using 1 M $LiPF_6$ in EC: DMC (1:1 by Vol% with 5% FEC) as the electrolyte. (b) Cyclic voltammetry curves of the first three cycles of Ni_2P anode at 0.1 mV s^{-1}.

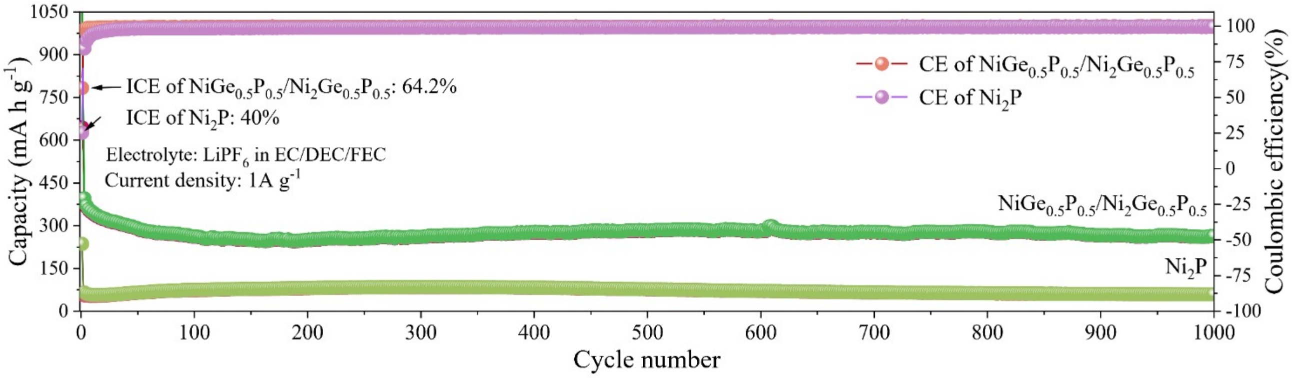

Fig. S7. cycle performance of the Ni_2P and $NiGe_{0.5}P_{0.5}/Ni_2Ge_{0.5}P_{0.5}$ anode at a current of 1 A g^{-1}.

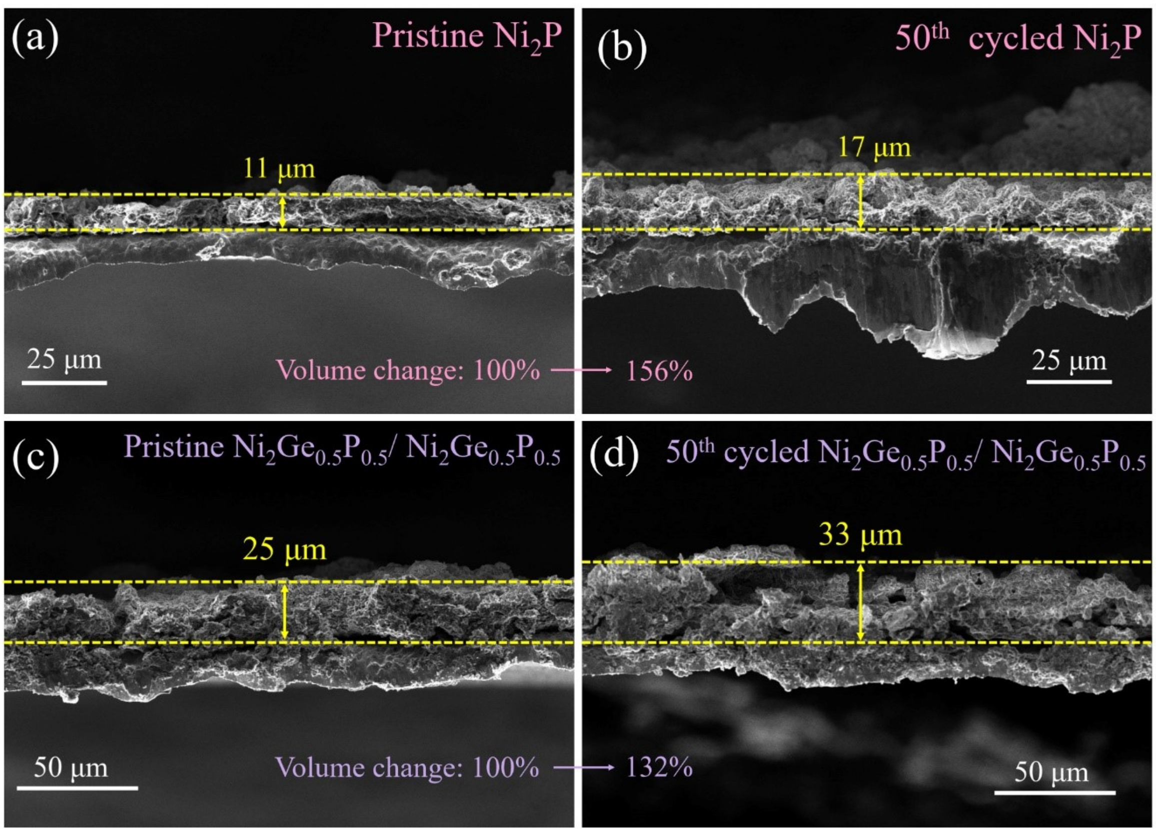

Fig. S8. Cross-sectional SEM images of the (a) Ni_2P electrode, (b) 50th cycled Ni_2P electrode, (c) $NiGe_{0.5}P_{0.5}/Ni_2Ge_{0.5}P_{0.5}$ electrode, and (d) 50th $NiGe_{0.5}P_{0.5}/Ni_2Ge_{0.5}P_{0.5}$ cycled electrode.

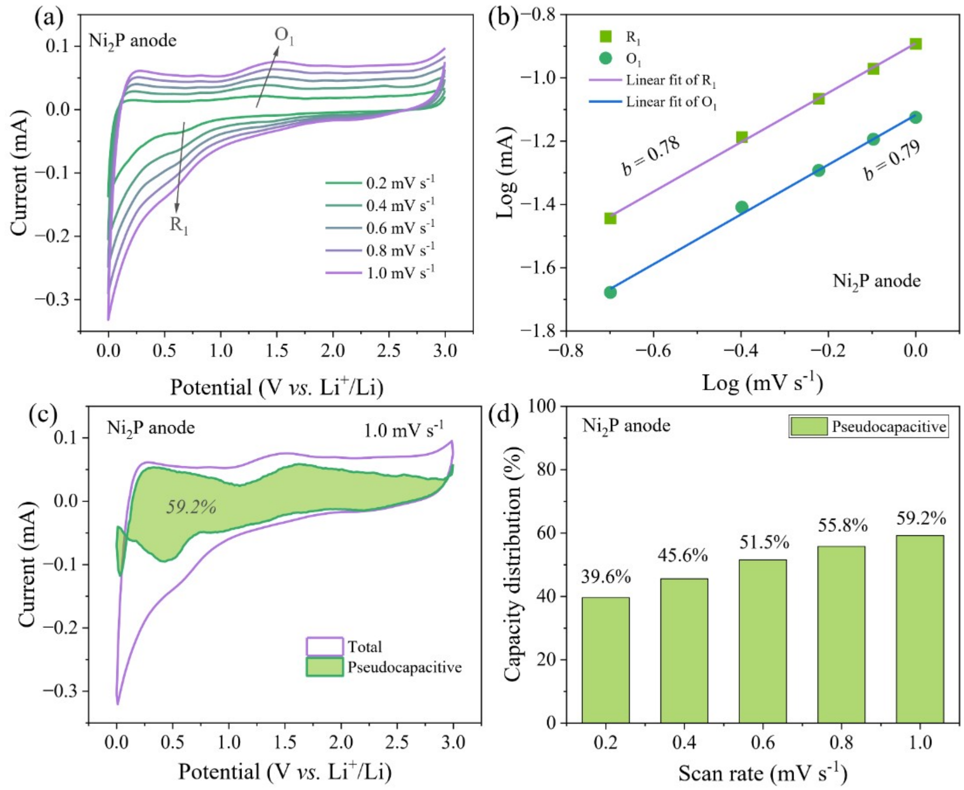

Fig. S9. (a) CV curves at different scan rates of Ni_2P. (b) The corresponding log(i) vs log(v) plots. (c) CV curve with pseudocapacitive contribution at 1.0 mV s^{-1} (d) Normalized ratio of pseudocapacitive and diffusion-controlled contribution at different scan rates.

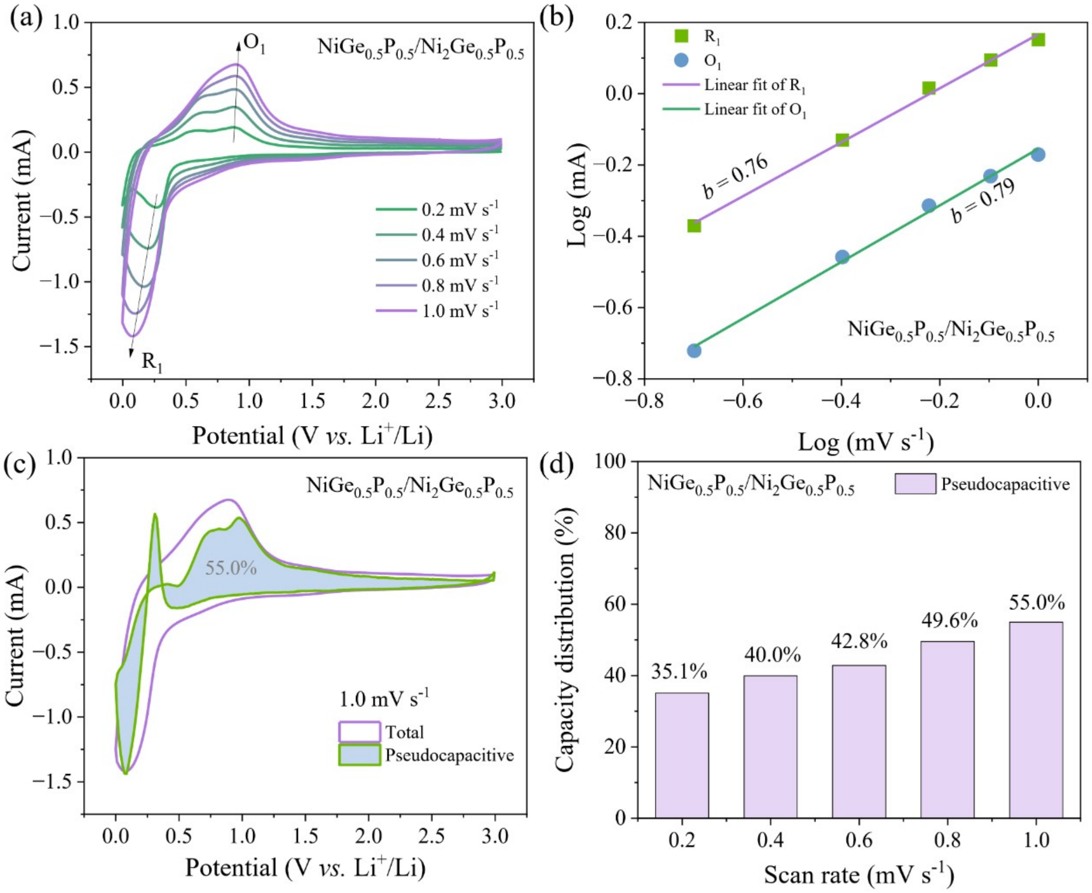

Fig. S10. (a) CV curves at different scan rates of $NiGe_{0.5}P_{0.5}/Ni_2Ge_{0.5}P_{0.5}$. (b) The corresponding log(i) vs log(v) plots. (c) CV curve with pseudocapacitive contribution at 1.0 mV s^{-1} (d) Normalized ratio of pseudocapacitive and diffusion-controlled contribution at different scan rates.

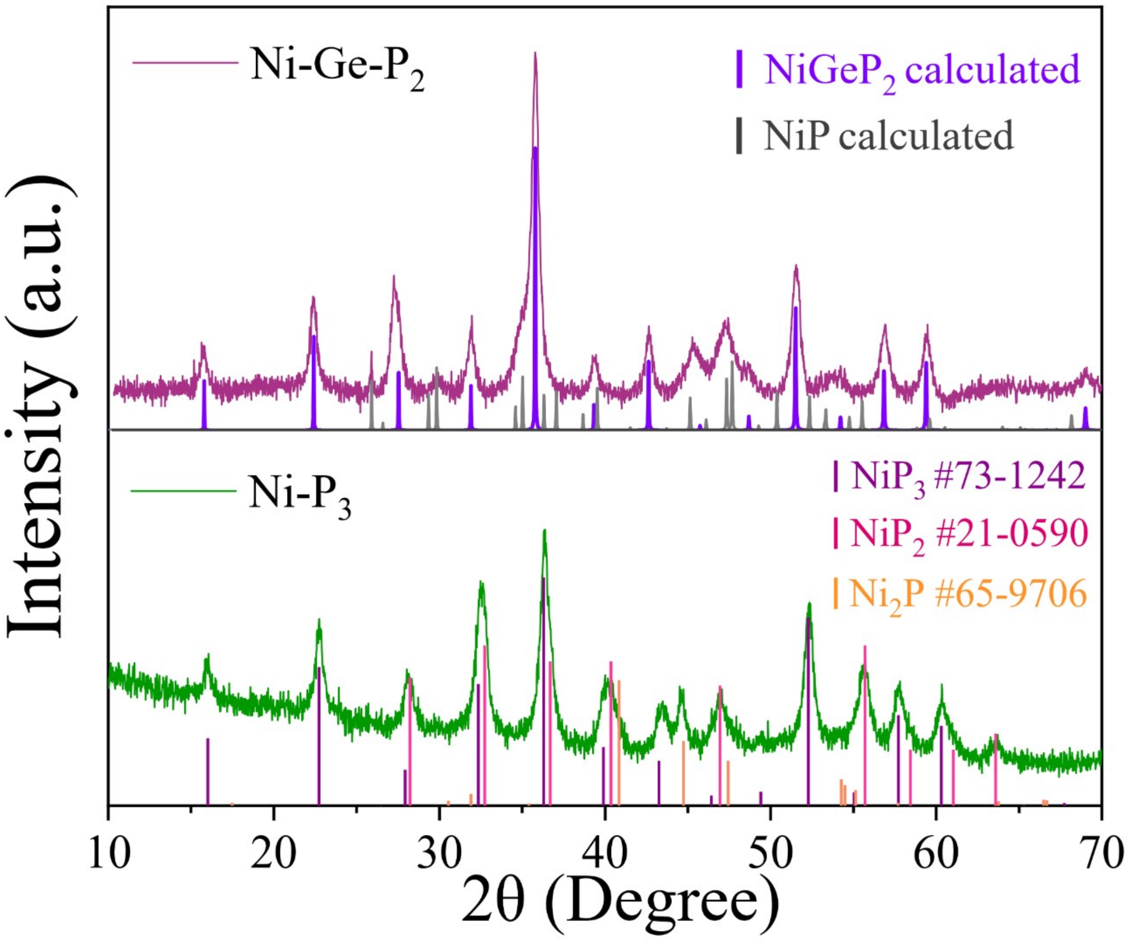

Fig. S11. XRD results of ball milled Ni-P_3 and Ni-Ge-P_2.

Table S4. Structure parameters for $NiGeP_2$ and NiP as determined by Rietveld refinement of powder XRD data at room temperature.

$NiGeP_2$:

Atom	Wyckoff site	*x*/a	*y*/b	*z*/c	Occupancy
Ni	8c	0.25	0.25	0	1
Ge	24g	0.34218	0.13511	0	0.3333
P	24g	0.34218	0.13511	0	0.6667
Space group: Im-3 (204); $a = b = c = 7.9284$ Å, $\alpha = \beta = \gamma = 90°$, *wt.*% = 78.13%.					

NiP:

Atom	Wyckoff site	*x*/a	*y*/b	*z*/c	Occupancy
Ni	8c	0.04077	0.57306	0.20326	1
P	8c	0.2406	0.62704	0.57452	1
Space group: P-62m (189); $a = 4.9446$, $b = 6.8736$ Å, $c = 6.0831$ Å, $\alpha = \beta = \gamma = 90°$, *wt.*% = 21.87%.					

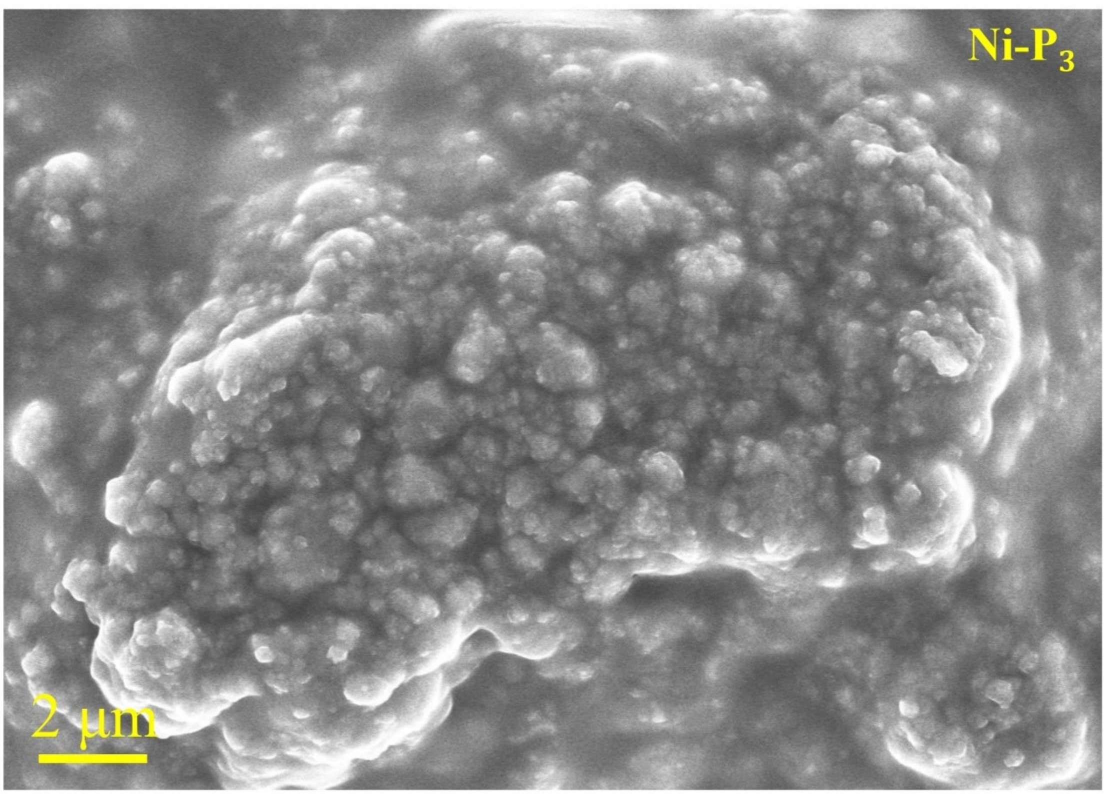

Fig. S12. SEM image of the ball-milled Ni-P_3

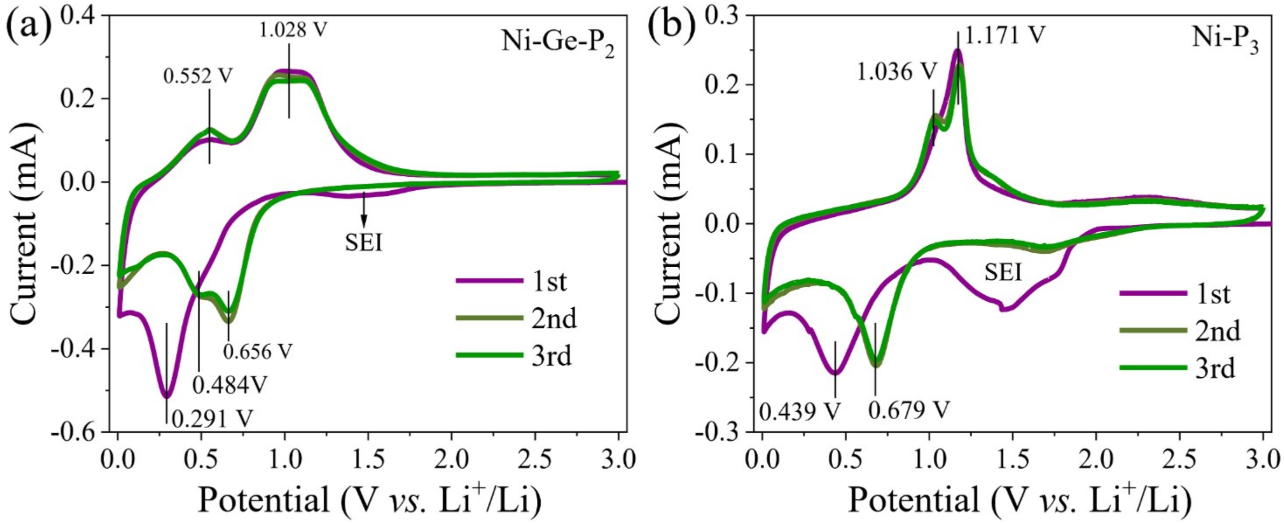

Fig. S13. Cyclic voltammetry curves of the first three cycles of (a) Ni-Ge-P$_2$ and (b) Ni-P$_3$ anode at 0.1 mV s^{-1}.

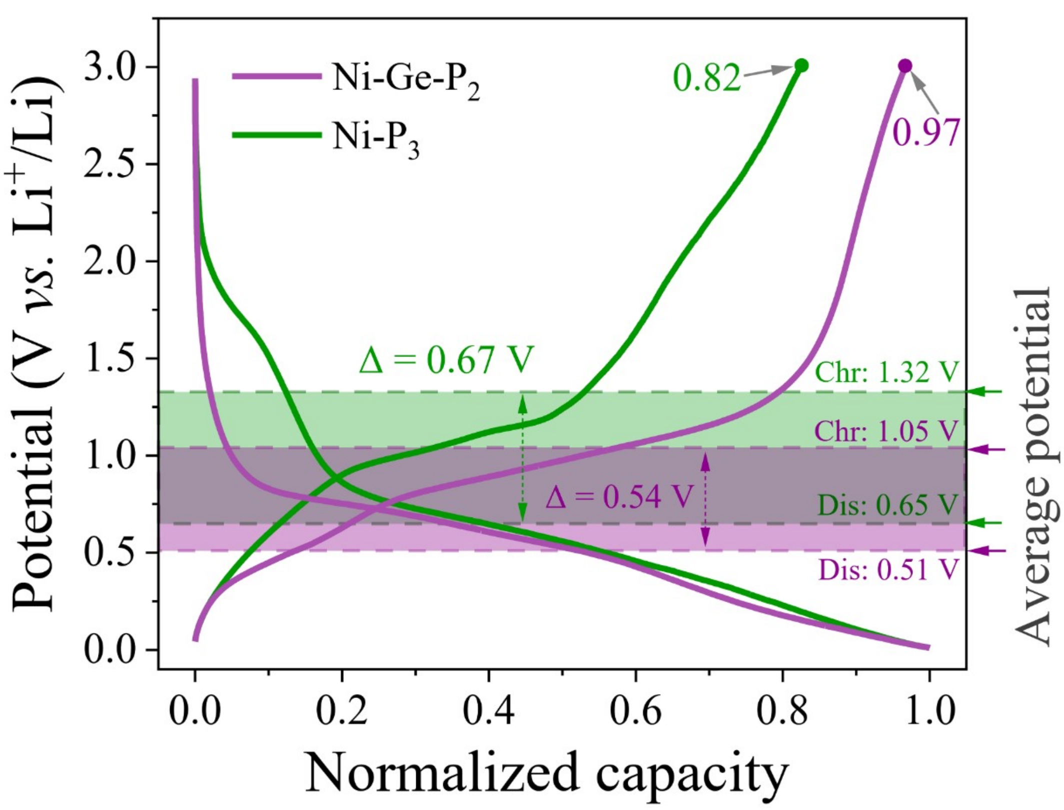

Fig. S14. Normalized charge−discharge curve comparison of the Ni-P$_3$ *vs.* Ni-Ge-P$_2$ at third cycle with average discharge/charge potential and polarization gap.

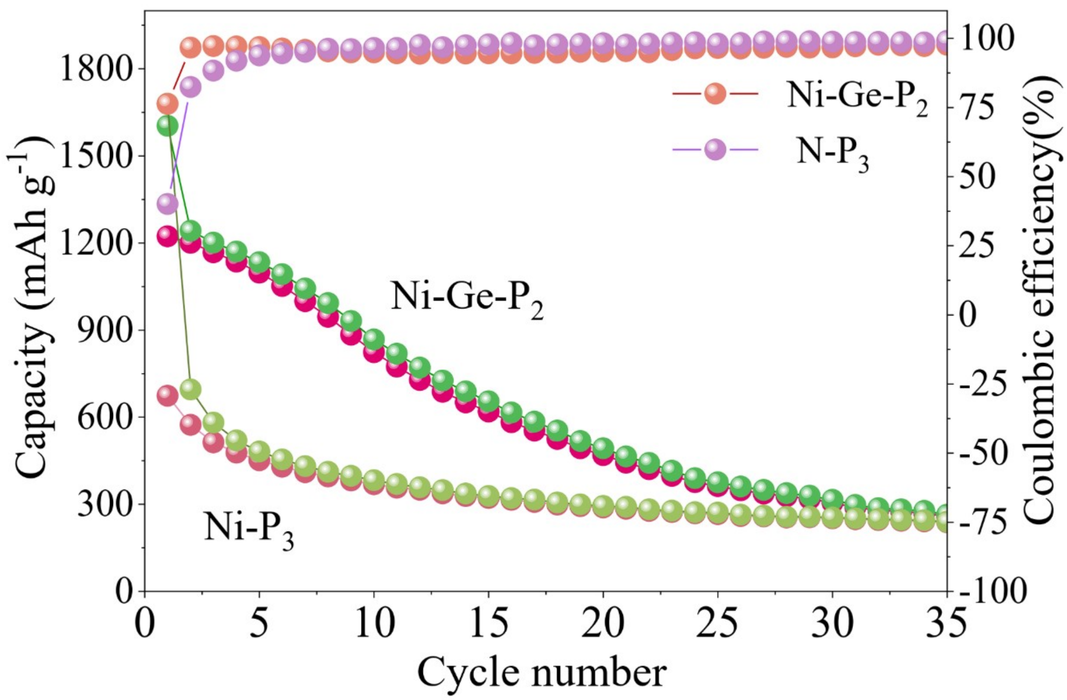

Fig. S15. Cycle performance of the Ni-Ge-P_2 and Ni-P_3 anode at a current density of 50 mA g^{-1}.

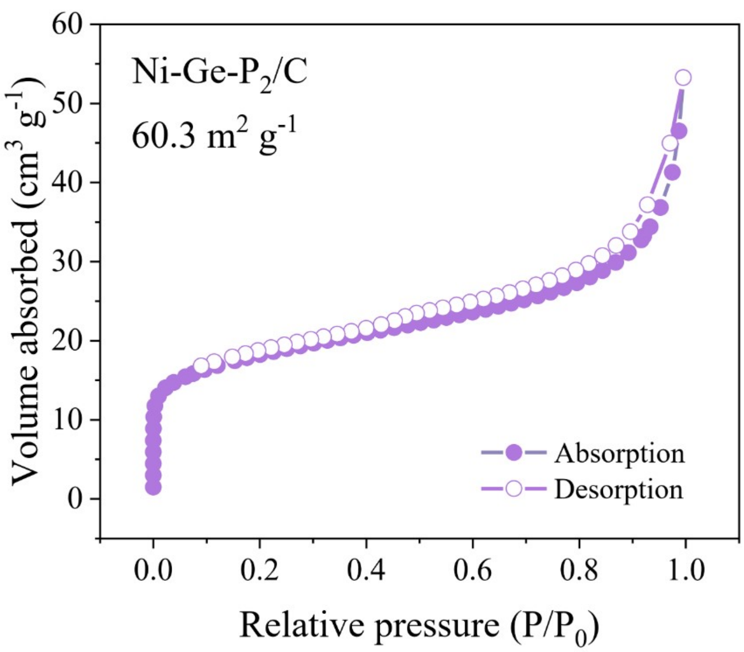

Fig. S16. BET-N_2 adsorption/desorption isotherm of Ni-Ge-P_2/C.

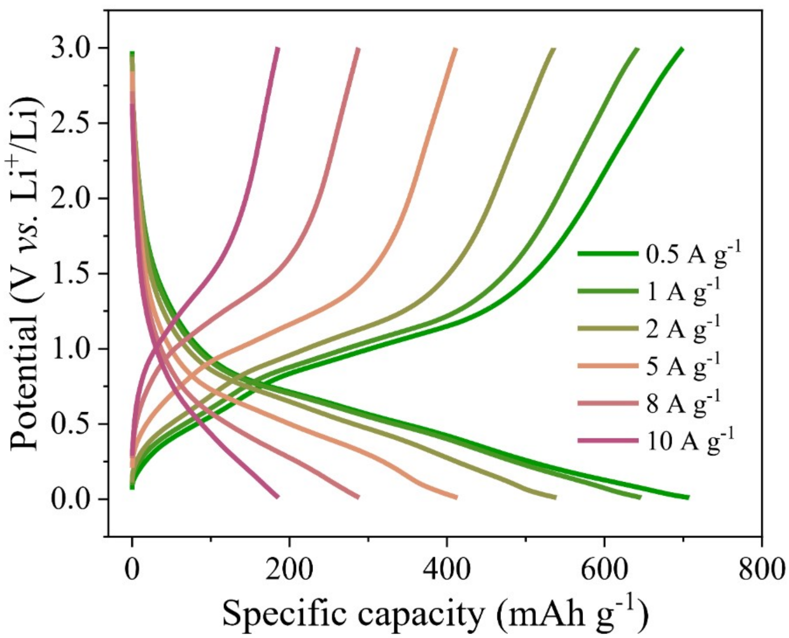

Fig. S17. Discharge–charge curves of the Ni-Ge-P_2/C at 0.5–10 A g^{-1}.

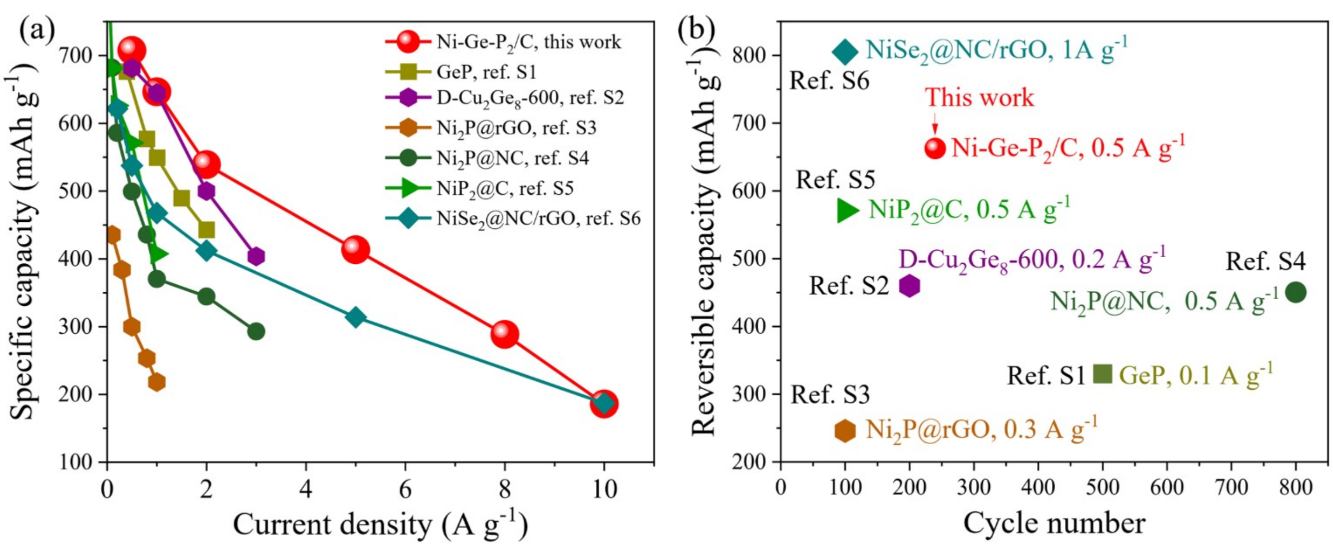

Fig. S18. (a) Rate and (b) cycling performance comparison of the Ni-Ge-P_2/C and previously reported Ni-, Ge-, and P-based anode.[1-6]

References

1. Y. Wei, X. Liu, Y. Zhang, R. Yao, T. Zhai and H. Li, Synthesis and Fast Exfoliation of Layered GeP Nanosheets for Advanced Li-Ion Batteries, *ACS Appl. Energy Mater.*, 2022, DOI: 10.1021/acsaem.2c03214.
2. Z. Zhang, K. Sun, Y. Chen, H. Yang, G. Xie, Z. Yu, M. Zhang, Y. Zhang, W. Li, S. Chou and Y. Jiang, High Conductivity Cu_3Ge and High-Capacity GeO_2 Synergistically Enhance a Continuous Channel Ge-Based Anode for Lithium-Ion Batteries with Long-Life and Scalable Preparation, *Energy & Fuels*, 2022, **36**, 13390-13397.
3. G. Cai, Z. Wu, T. Luo, Y. Zhong, X. Guo, Z. Zhang, X. Wang and B. Zhong, 3D hierarchical rose-like Ni_2P@rGO assembled from interconnected nanoflakes as anode for lithium ion batteries, *RSC Adv.*, 2020, **10**, 3936-3945.
4. S. Tao, P. Cui, S. Cong, S. Chen, D. Wu, B. Qian, L. Song and A. Marcelli, Metal-organic framework-derived Ni_2P/nitrogen-doped carbon porous spheres for enhanced lithium storage, *Sci. China Mater.*, 2020, **63**, 1672-1682.
5. G. Li, H. Yang, F. Li, J. Du, W. Shi and P. Cheng, Facile formation of a nanostructured NiP_2@C material for advanced lithium-ion battery anode using adsorption property of metal–organic framework, *J. Mater. Chem.*, 2016, **4**, 9593-9599.
6. Q. Liu, B. Chen, W. Liang, Y. Xu, G. Li, L. Shao, X. Shi and Z. Sun, Multi-heteroatom-Doped Carbon Matrix and N-Doped Carbon Shell Double Protection Enabled Superb Stability of Nickel Diselenide for Lithium Storage, *ACS Appl. Energy Mater.*, 2022, DOI: 10.1021/acsaem.2c03051.